

Article

Surface Displacement and Source Parameters of the 2021 Bandar-e Genaveh, Iran, Earthquake Determined from InSAR Observations

Zeinab Golshadi ^{1,*}, Nicola Angelo Famiglietti ² , Simone Atzori ²  and Annamaria Vicari ² ¹ Institute of Geophysics, University of Tehran, Tehran 141556466, Iran² Istituto Nazionale di Geofisica e Vulcanologia, 605, 00143 Rome, Italy; nicola.famiglietti@ingv.it (N.A.F.); simone.atzori@ingv.it (S.A.); annamaria.vicari@ingv.it (A.V.)

* Correspondence: z.golshadi@alumni.ut.ac.ir; Tel.: +98-919-2906-527

Abstract: On 18 April 2021, a M_W 5.8 earthquake occurred near the city of Bandar-e Genaveh, southwestern Iran. Four synthetic aperture radar (SAR) images, acquired from Sentinel-1 (ESA Copernicus project) satellites in ascending and descending orbits, were used to get two displacement maps, catching the surface co-seismic effects through the two-pass InSAR technique. Modeling the deformation patterns using equations for a shear dislocation in elastic half-space allowed the source parameters and the slip distribution of the seismogenic source to be determined. We calculated that the rupture occurred on a reverse fault extending NW-SE, gently dipping NE and with a maximum slip reaching about 1 m. The northeast and low-dip angle of this fault are also consistent with the tectonics of the region, which is subject to deformation and shortening along the northern margin of the Arabian plate. Our estimations of the fault parameters agree with the Zagros Foredeep reverse fault. We additionally processed four other SAR images to investigate the possibility that the M_w 5.0 aftershock, which occurred about one month later, induced surface effects visible with InSAR. This analysis, however, did not provide any clear conclusions.

Keywords: Genaveh earthquake; co-seismic deformation; Sentinel-1 A; interferometric synthetic aperture radar; geodetic modeling



Citation: Golshadi, Z.; Famiglietti, N.A.; Atzori, S.; Vicari, A. Surface Displacement and Source Parameters of the 2021 Bandar-e Genaveh, Iran, Earthquake Determined from InSAR Observations. *Appl. Sci.* **2022**, *12*, 4223. <https://doi.org/10.3390/app12094223>

Academic Editors: Filippos Vallianatos and Vassilis Sakkas

Received: 19 March 2022

Accepted: 17 April 2022

Published: 22 April 2022

Publisher's Note: MDPI stays neutral with regard to jurisdictional claims in published maps and institutional affiliations.



Copyright: © 2022 by the authors. Licensee MDPI, Basel, Switzerland. This article is an open access article distributed under the terms and conditions of the Creative Commons Attribution (CC BY) license (<https://creativecommons.org/licenses/by/4.0/>).

1. Introduction

On 18 April 2021, at 6:41 UTC (11:11 Iran Standard Time), a M_W 5.8 earthquake occurred near the city of Bandar-e Genaveh, in the seismically active area of the Bushehr province, southwestern Iran (Figure 1). This earthquake occurred in the strongly active area, with structures oriented mostly northwest-southeast and dominated by right-slip and reverse fault mechanisms [1,2]. It did not cause casualties, extensive damage or surface ruptures in the affected area [3]. There were 200 aftershocks following this earthquake over the next 4 months, with 20 of a magnitude higher than 4 [4]. Among them, a large aftershock of M_w 5.0 occurred on May 21, potentially causing additional surface displacements.

A number of studies have investigated this earthquake using finite fault modeling (Table 1) based on different techniques. However, there are inconsistencies between the different fault models. According to the Harvard group and the U.S. Geological Survey (USGS), the Global Centroid Moment Tensor (GCMT) solution is a fault-plane solution that is consistent with nearly thrust-slip motion, but the USGS solution prefers a smaller seismic moment release.

In order to reconstruct the complex active fault system of the investigated area, we exploit the InSAR (Interferometry from Synthetic Aperture Radar) two-pass technique, a well-consolidated instrument to retrieve the surface deformations [5]. InSAR is, indeed, a geodetic technique capable of obtaining high resolution displacement maps with centimetric accuracy over a wide area [6]. These maps reveal the displacement in LoS (Line-of-Sight)

direction, i.e., the line connecting the satellite to the pixel on the ground, and they can be used, through a geophysical model and optimization algorithms, to derive the parameters of the source responsible for the earthquake [7]. Given the peculiar geometry of the LoS direction, the combination of images acquired from ascending and descending orbits is generally preferred to better constrain the deformation field and, consequently, the source parameters.

Table 1. Source parameters of the 2021 Genaveh earthquake.

Reported by	Dataset	Magnitude	Plane No.	Strike (°)	Dip (°)	Rake (°)	Depth (km)	latitude (°)	longitude (°)
USGS	Teleseismic	5.8 (M_{WW})	1	308	28	80	8	29.753	50.678
			2	139	62	95			
GCMT	Teleseismic	5.9 (M_w)	1	300	26	79	12	29.61	50.60
			2	132	65	95			
IGUT	Regional seismic data	5.9 (M_w)	Mainshock	-	-	-	9	29.73	50.67
		5 (M_n)	aftershock	-	-	-	9	29.79	50.57
IIEES	Regional seismic data	6 (M_L)	-	-	-	-	20	29.71	50.70
RHDRC	Local seismic data	6 (M_W)	-	-	-	-	10	50.79	29.79
EMSC	Regional seismic data	5.8 (M_W)	-	-	-	-	10	50.70	29.82
GFZ	Teleseismic	6 (M_W)	-	-	-	-	10	50.66	29.77

USGS: United States Geological Survey; GCMT: Global Centroid Moment Tensor; IGUT: Institute of Geophysics, University of Tehran; IIEES: International Institute for Earthquake Engineering and Seismology; RHDRC: Road, Housing and Development Research Center; EMSC: European-Mediterranean Seismological Centre; GFZ: German Research center for Geosciences.

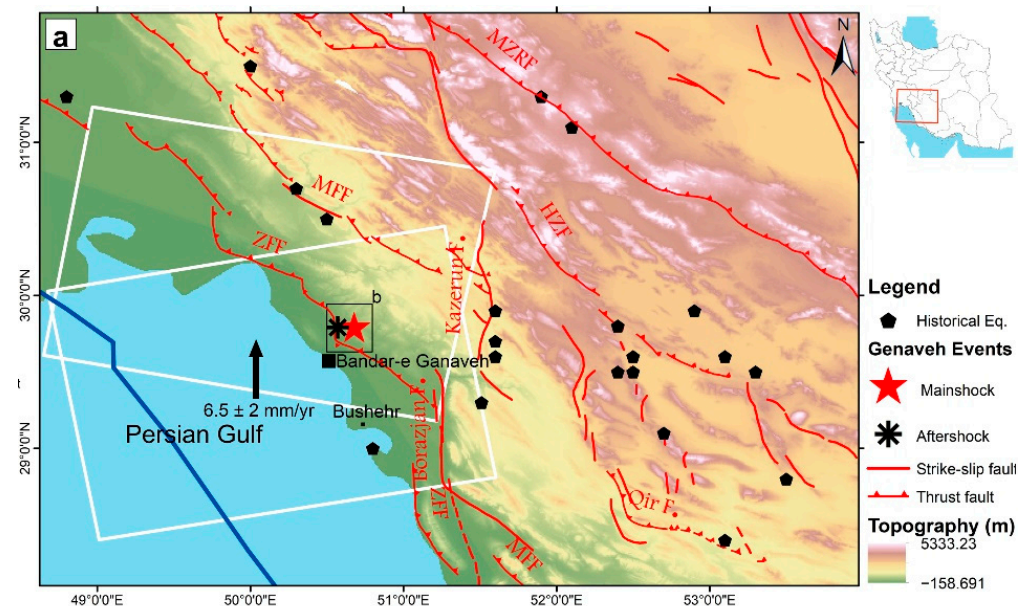


Figure 1. Cont.

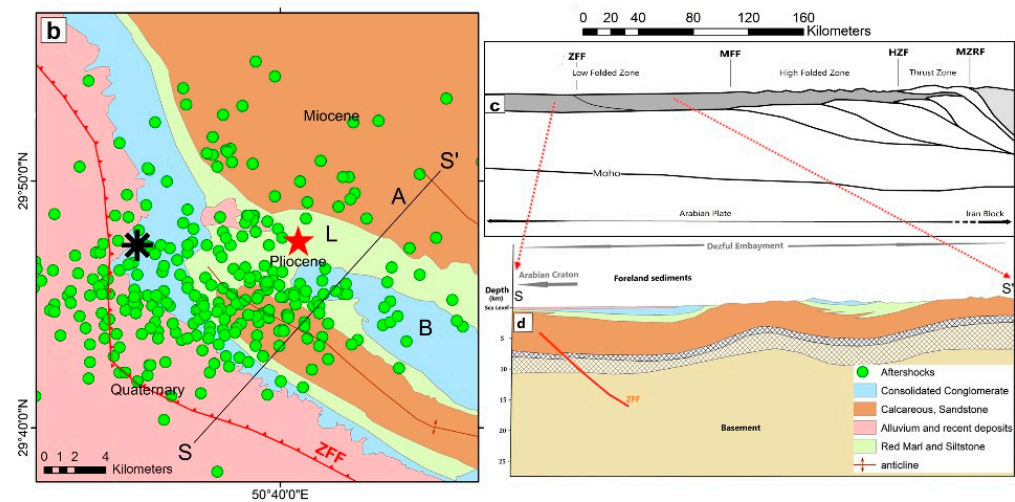


Figure 1. (a) Map of the investigated area plotted on shaded relief map of SRTM digital elevation model; red star represents the location of the 18 April 2021, M_W 5.8 mainshock and the black one indicates the 21 May 2021, M_W 5.0 aftershock [4]; black pentagons indicate historical earthquakes [8]; white rectangles mark the footprints of Sentinel-1 images used in this work; red lines are the active faults in the area [9,10]. Abbreviations are; ZFF-Zagros Foredeep Fault, HZF-High Zagros Fault, MFF-Mountain Front Fault and MZRF-Main Zagros Reverse Fault. Dark blue line show boundaries of cratons and tectonic belts as deformation front [11]. (b) Zoom on the investigated area, with the geological map [12]. The ZFF fault extends through sedimentary rocks and cuts simple folding of Bakhtiari, Lahbari, Aghajari formations (B, L and A labels in figure, respectively) [13]; Arrow shows the relative velocity of Arabia with respect to Eurasia in mm/year [14]; green circles indicate aftershocks up to 15 July 2021. (c) A simplified cross-section through northeast to southwest of (a) [15–17]. (d) Geological profile of SS' in (b) and enlarged (c) section [10,13].

In this study, we infer the source of the 2021, M_W 5.8, Genaveh earthquake through the modeling of ascending and descending InSAR displacement data, providing the fault geometries, kinematics and the slip distribution for the mainshock. We also investigate how the convergent tectonics of this region relate to the obtained causative fault. We additionally investigate the possibility that the M_W 5.0 aftershock induced some co-seismic surface effects by calculating and modeling two more InSAR displacement maps. The outcome of this analysis, however, did not provide an evident conclusion.

Geological and Tectonic Setting

This area is located in southwestern Iran, within the complex Neogene collision zone between the Arabian and Eurasian plates, with a tectonic shortening rate of approximately 6.5 ± 2 mm/yr [14] as a result of post-collisional crustal shortening that is transferred to the foreland structures and ophiolite obduction [18,19] (Figure 1).

This area is one of the most seismically active intra-continental fold-and-thrust belts on Earth. Zagros Mountains and their coupled foreland basin were evolved during a multi-episodic orogeny from the Late Cretaceous to recent times [20]. The estimated σ_1 axis in Zagros Folded and thrust Belt (ZFTB) trend rotates in anti-clockwise direction from NE-oriented trajectories to the southeast to ~N-oriented trends to the north [10]. There are four major active faults in ZFTB, which are the Zagros Foredeep Fault (ZFF), the High Zagros Fault (HZF), the Mountain Front Fault (MFF) and the Main Zagros Reverse Fault (MZRF). Most of these faults trend NW–SE and NNW–SSE, with dips of 30–60° and rakes of 60–120° along the plate boundary [9,21]. There is an older sequence of deformation in the inner parts of Zagros chain and a younger sequence in the outer Simply Folded Belt since the Late Cretaceous to Pliocene period [17].

In this region, several tectonic units are divisible from northeast to southwest with non-uniform deformation [10]. Tectonic slices of the highly deformed domain of thrust

zone, including the Arabian margin, remains of island arcs, fragments of Cretaceous ophiolites and accretionary prisms, developed above a basal detachment in the latest Neoproterozoic–Lower Cambrian Hormuz evaporates or lateral equivalent [17,20,22]. In the Zagros belt, the deformation and tectonic process that reactivated the Late Cretaceous–Paleogene obduction belt is characterized by thin- and thick-skinned tectonics [17]. Tectonic deformation of the Zagros foreland basin was closely related to the propagation of faults from the Arabia–Eurasia suture zone to the southwestern side [22]. The Simply Folded Belt, limited by the HZF and the MFF, is characterized by many elongated anticlines. The low folded zone, located to the southwest of the MFF (Figure 1b), is characterized by a series of elongate folds of Miocene strata [23]. Multi-detachment folds with subordinate thrusting characterize the deformation of the sedimentary cover of the Arabian margin [24]. According to the progressive limb rotation model of fold kinematics, these formations are growth strata which accumulated during folding. As a result of folding, N- and NW-trending basement faults accommodated shortening [10]. Multiplicity of decollement levels promotes a partly decoupled deformations and limits the size of most faults in the area [19,24].

The Dezful embayment changes the obliquity of Arabian plate convergence, controls the slip rate of faults, and contributes to the formation of the ZFTB [10]. The study area is bounded by the Zagros Foredeep Fault (ZFF) and the Borazjan fault. Inverse ZFF is generally northwest–southeast with a slope to the northeast [1]. It separates the foredeep Zagros belt (north and northeast) from the Quaternary alluvium of the Persian Gulf coastal plain (south and southwest) and in the form of overthrust fault branches, has cut the folds in the region [1]. The strike-slip segment of the Kazerun Fault displaced the High Zagros Fault southward [10]. The ZFF has been extended as a dextral fault along the active Kazerun–Borazjan fault for 105 km and is composed of various hidden fault segments that partition the compressional structures within this range. This fault, like the MFF with a predominant thrust regime and the HZF with a combination of thrust and strike-slip regimes [10], is a deep fault that, after cutting the sedimentary cover of the upper crust, extends to the lowest parts of the crust and reaches the shear zone to Moho. As a result of the thrust Borazjan fault activation, the fold axis has curved, elongated, and dislocated across the Zagros belt as dextral [25] (Figure 1). Under NE dip low-angle basal thrusts, Arabian basement rocks are deformed by large crustal thrusts that actually merge at depth and correspond to the uppermost crystalline basement [24].

2. Methodology

2.1. InSAR Observations and Processing

In this work, we used Sentinel-1 (ESA Copernicus project) data in Interferometric Wide (IW) swath mode to retrieve the ground displacement field induced by the Genaveh earthquake; it acquires data with a 250 km swath at a 5 m by 20 m spatial resolution (single look). IW mode captures three sub-swaths using Terrain Observation with Progressive Scans SAR (TOPSAR). A white rectangle in Figure 1 indicates the footprints of SAR images covering the area of the event. We generated four interferograms, each with a temporal baseline of 12 days, to measure the mainshock and the M_W 5.0 aftershock deformations, both from ascending and descending orbits (Table 2).

Table 2. Sentinel-1 pairs used to detect the permanent deformations of the Genaveh mainshock and the aftershock.

Event	Interferogram Number	Master Date	Slave Date	Pass Direction	Orbit Number	Normal Spatial Baseline (m)	Temporal Baseline (Day)
Mainshock	1	14 April 2021	26 April 2021	Ascending	101	41.21	12
	2	10 April 2021	22 April 2021	Descending	35	39.18	12
Aftershock	1	20 May 2021	01 June 2021	Ascending	101	6.73	12
	2	16 May 2021	28 May 2021	Descending	35	39.92	12

Co-seismic processing was carried out with ENVI[®] SARscape[®] (Sarmap, CH, Version 5.5, distributed by HARRIS Geospatial Solutions, Switzerland, Retrieved from <http://www.sarmap.ch/>) software, using the two-pass InSAR method to produce the interferograms [26]. The Shuttle Radar Topography Mission (SRTM) digital elevation model (DEM) with 30 m resolution (Available online: <https://earthexplorer.usgs.gov/> (accessed on 5 May 2021)) was used to remove the topographic phase contributions [27], precise orbits (Available online: <https://qc.sentinel1.eo.esa.int> (accessed on 19 May 2021)) were used for orbital corrections and the Goldstein filtering method was also applied to wrapped fringes [28] to reduce the interferometric phase noise. A phase unwrapping and displacement maps were created using the minimum cost flow (MCF) algorithm [29] and the slant range maps were eventually geocoded to UTM zone 39, with a pixel size of 30 m. The interferograms and the displacement maps are shown in Figure 2; due to the favorable conditions (dry soil, short temporal and spatial baselines), the interferometric coherence is very high and the coverage is continuous.

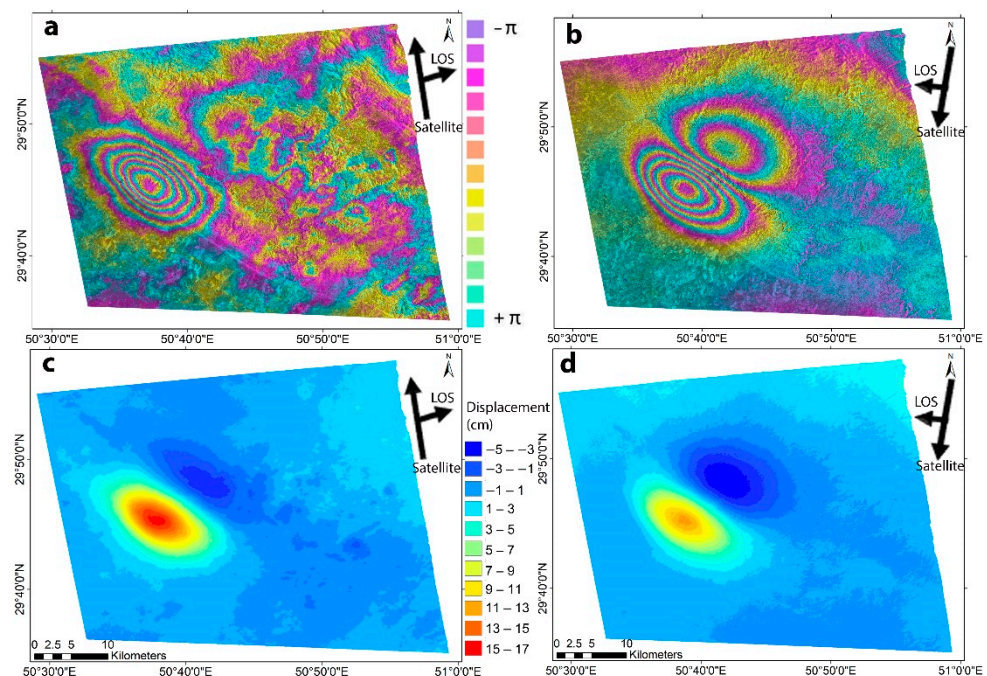


Figure 2. Interferometric fringes (a,b) and displacement maps (c,d) for ascending (left) and descending (right) orbits for the 2021 Genaveh mainshock. Positive displacement indicates a movement toward the satellite (e.g., uplift), whereas negative displacement indicates a movement away from the satellite (e.g., subsidence).

We also considered the possibility that the M_W 5.0 occurred on May 21st induced a detectable surface effect; the two displacement maps, obtained from the processing of images listed in Table 2, are shown in Figure 3. The two maps show a small, but clear, signal of a few centimeters that can be ascribed to several different causes, and we will investigate through their modeling in the next section.

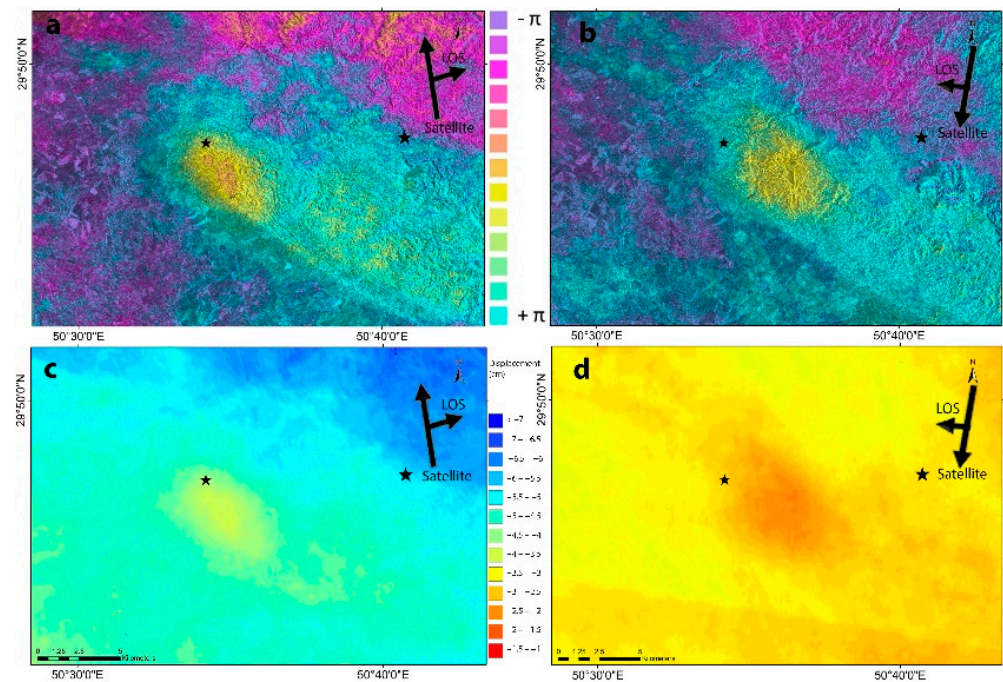


Figure 3. Ascending (a,c) and descending (b,d) pattern of Interferometric fringes and displacements including the May 21, M 5.0 aftershock. The biggest dark star indicates the location of the mainshock and the small dark star shows the location of May aftershock.

2.2. Elastic Dislocation Modelling Using InSAR Observations

To provide an accurate estimate of the earthquake source parameters based on a single rectangular fault plane and to determine where in-depth slip distributions are located, the following analysis of InSAR data and modelling was performed. After processing the four interferograms of Table 2, we started the modeling of displacement data to get the source parameters. In order to reduce the amount of data to handle in the inversion, particularly needed in this area where the radar coherence is maximized, we sampled the InSAR raster maps adopting a regular grid sampling of 2000 m in the far field and 500 m in the near field. With this sampling, we obtained a subset of 3500 points for the ascending and descending datasets. Then, co-seismic displacement modeling was conducted using a consolidated two-step inversion method: a non-linear inversion to solve for the geometry, location and uniform shear dislocation on a rectangular source, and a linear inversion to solve for the slip distribution over the constrained fault plane [30]. In both steps, the underlying model is the rectangular shear dislocation in a homogeneous and elastic half-space [31]. Further, we adopt a strategy to account for the effects of topography [32], ranging in this area from zero to around 600 m and playing a small but not negligible role. For every event, we jointly inverted the ascending and descending displacement maps. The non-linear inversion exploits the Levenberg–Marquardt minimization algorithm to find the global minimum of the cost-function based on the least-squares of the residual between the observed and predicted data [33]; it consists of a Gauss–Newton method, implemented with multiple restarts to guarantee catching of the global minimum. Details of the implementation can be found in [30].

After the definition of the source geometry with a uniform slip and rake, we calculated the slip distribution along the fault plane, by using the algorithm described in [34]. It consists of a least squares optimization based on linear inversion of the matrix:

$$\begin{bmatrix} d_a \\ d_d \\ 0 \end{bmatrix} = \begin{bmatrix} G \\ k \cdot \nabla^2 \end{bmatrix} \cdot m$$


where d_a and d_d are the observed ascending and descending data vectors, respectively, m is the vector of the unknown slip values, G is the Green's function matrix, ∇^2 is a Laplacian operator used to regularize the slip distribution, weighted by the empiric coefficient k [35,36]. To prevent the change of the slip direction (back-slip) along the fault, we used additional constraints of non-negativity of the parameters.

We remark that all the inversions (non-linear and linear, for the mainshock and the aftershock) are carried out with a joint contribution of ascending and descending InSAR datasets, automatically weighted according to the approach described in [37]. Furthermore, for every inversion the parameters of a possible ramp that affects the InSAR data were simultaneously assessed together with the source parameters.

3. Results

The displacement maps show a peak of about 0.17 and 0.13 m, from ascending and descending orbits, respectively (Figure 2). Positive values indicate a displacement toward the satellite, in the LoS, which reflect the presence of the uplift typical of thrust earthquakes. In fact, a few centimeters of variation in LoS displacement measurements might also be related to the different viewing angles between the ascending and descending satellite observations, and the contribution of the horizontal (mainly E-W) motion component. In addition, the important difference between the two LoS, ascending and descending, witnesses the existence of an important horizontal component, as expected for this type of rupture that occurs along a low-dip plane. Table 3 shows the source parameters for the deformation constrained by the non-linear inversion of two maps containing the effects of the M_W 5.8 mainshock; it shows that the deformation was caused by a fault with 9.5 km in length, 5 km in width, 20° in dip, and 313° in strike with a prevalently inverse rupture mechanism with an average slip of about 0.7 m, consistent with the focal mechanism determined by USGS, as discussed in the next section.

Table 3. Fault parameters of the Genaveh mainshock after the non-linear inversion. Latitude and longitude refer to the source center, vertically projected to the surface; depth refers to the fault top edge. For every parameter, the 1-sigma uncertainty is reported within brackets.

Width (km)	Length (km)	Depth (km)	Strike ($^\circ$)	Dip ($^\circ$)	Longitude	Latitude	Rake ($^\circ$)	Slip (m)	Focal Mechanism
5.0 (0.3)	9.5 (0.1)	4.0 (0.1)	313 (1)	20 (1)	50.650 (0.001)	29.773 (0.001)	100 (2)	0.7 (0.1)	

To calculate the slip distribution of the source, using the linear inversion described in the previous section, we firstly extended the fault planes so that the source could include the entire slip distribution, from the peak value to zero, at the edges; the fault was then subdivided into patches of 1×1 km. According to the slip distribution (Figure 4), the maximum slip of approximately 1 m was located at a depth of 4.5 km; the slip distribution is constrained between a depth of 2.5 km and 6.0 km, thus confirming that the rupture did not reach the surface. The comparison of the observed and modeled displacements after the linear inversion is shown in Figure 5, along with a map of residuals; observed and predicted displacements differ by less than a centimeter on most of the map, but with very

localized fluctuations up to 3 cm, due to the unavoidable approximations introduced by the elastic model.

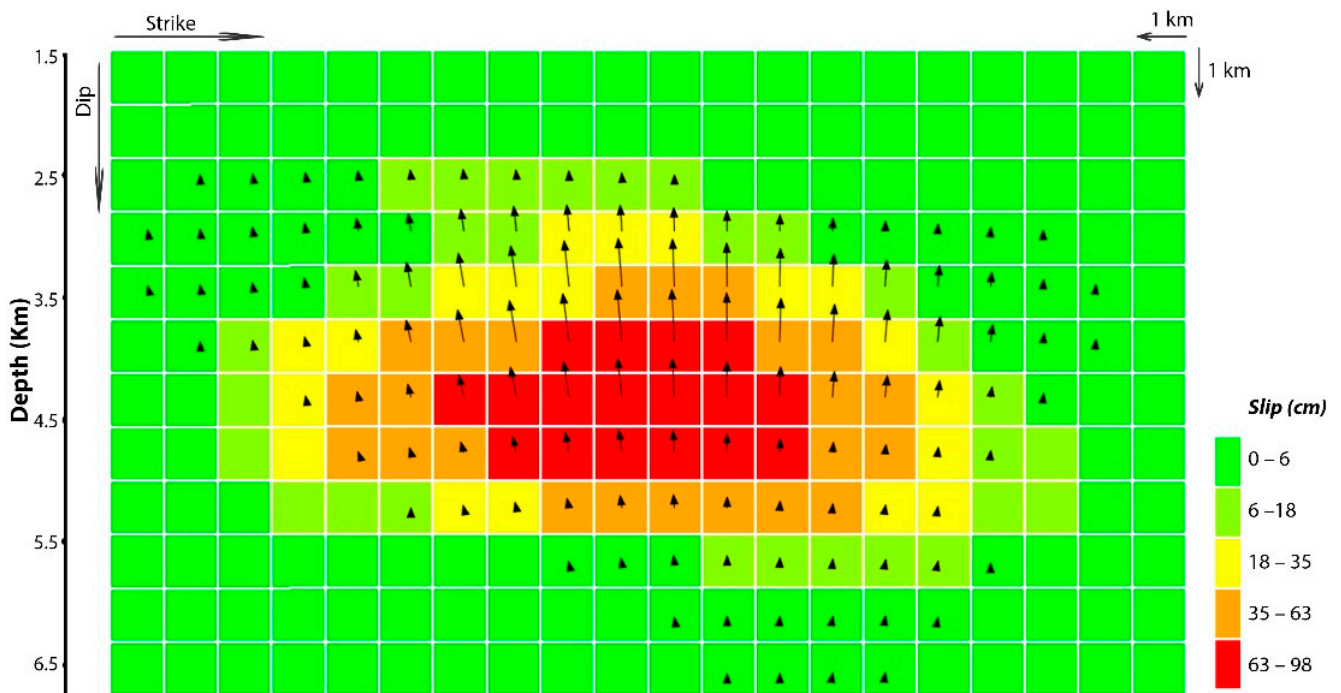


Figure 4. Slip distribution of the Mw 5.8 mainshock.

The geodetic moment corresponding to the slip distribution is 1.0×10^{18} Nm, close to the reported value of 6.7×10^{17} Nm by the USGS; the strike, dip and rake values retrieved through inversion (313° , 20° , 100°) are also in a good agreement with those calculated by the USGS (308° , 28° , 80°) and the Global CMT catalog (310° , 26° , 94°).

Additionally, we considered the hypothesis of constraining the source of the biggest aftershock, the M_W 5.0 event occurred May 21st, for which some deformation patterns were observed in both ascending and descending displacement maps (Figure 3). Though the displacement, from both orbits, has very low intensity (about 3 cm of maximum displacement), the location is close to the epicenter (Figure 3), suggesting a possible correlation of the signal with the seismic source. We therefore adopted the same modeling scheme used for the mainshock, in order to verify the compatibility of the detected signal with that predicted from a dislocation source. Unfortunately, no clear indications arose from the inversion: no fault configuration was found to unambiguously attribute the observed signal to a shear source. However, the presence of a similar pattern in both maps, obtained from completely independent image pairs, is unlikely to be caused by atmospheric artifacts, characterized by a very low correlation in time. It can be interpreted qualitatively as a post-seismic variation of the underlying volume, possibly caused by fluid migration.

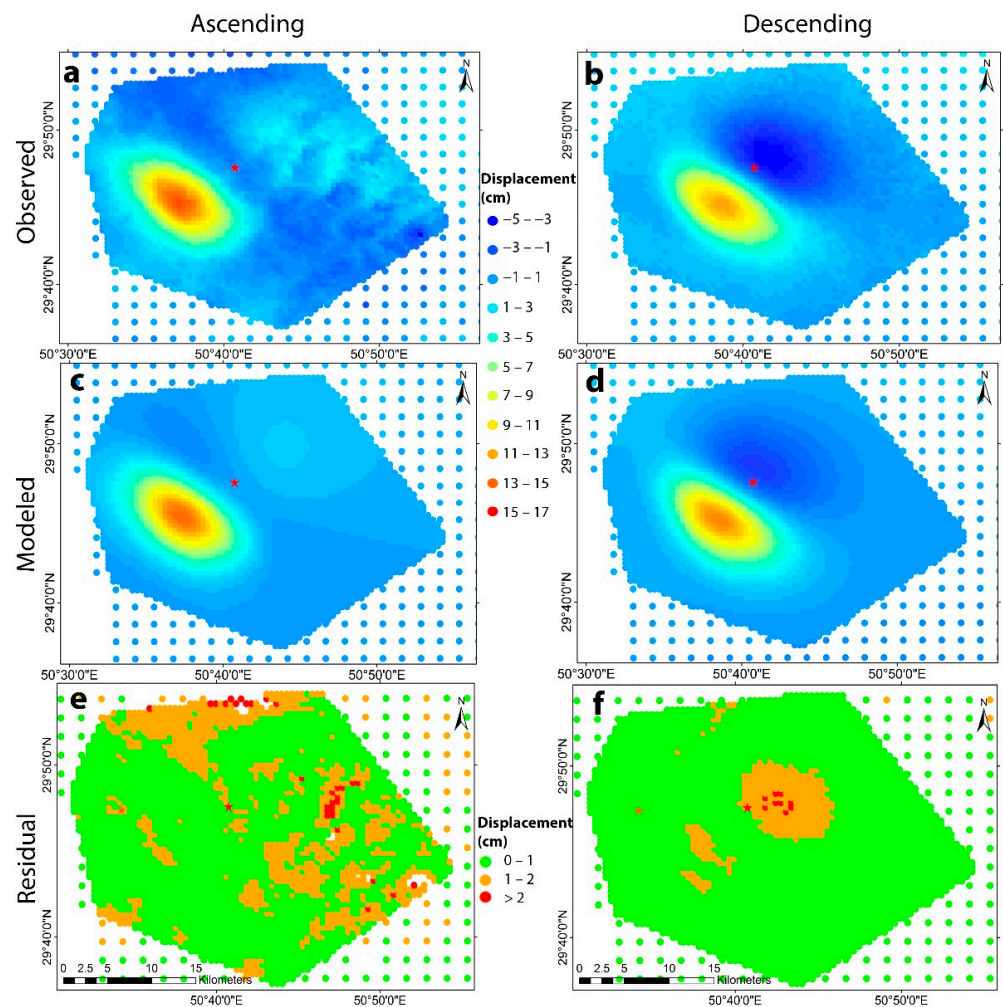


Figure 5. Observed, modeled and residual maps for displacements obtained from ascending and descending orbits for Mw 5.8 mainshock. The red star shows the location of mainshock.

4. Discussion and Conclusions

Geodetic observational data, such as InSAR measurements, are by now regularly used to infer information concerning sources of surface displacements and to understand the underlying processes. The significant co-seismic surface deformation signal of 18 April 2021, Bandar-e Genaveh earthquake, is clearly depicted by the InSAR images used in this study. The analysis of the mainshock co-seismic deformation demonstrated that the observed signal can be ascribed to a unique reverse fault with a 20° low dip to the northeast, across a broad ($\sim 9.5 \times 5$ km) rupture plane, corresponding to the pre-existing seismogenic thrust Zagros Foredeep Fault (Figure 6). In the southwest of Iran, it accommodates the convergence of low-depth values of density contrast discontinuity of the Arabian and Eurasian plates in the subduction zone [10,11].

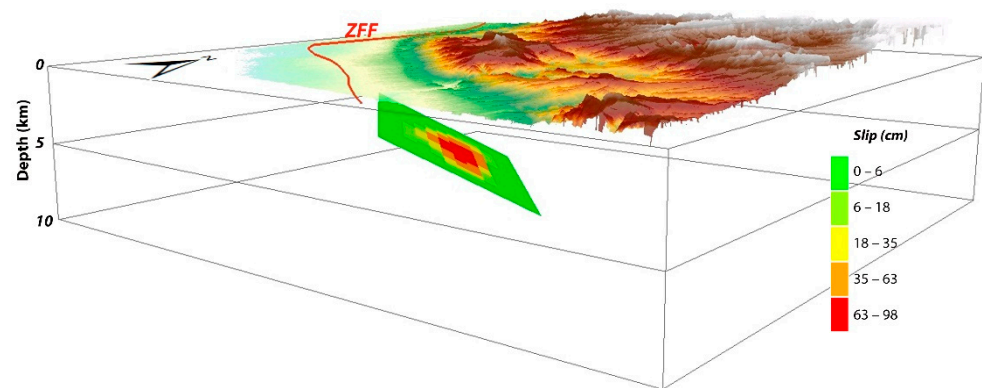


Figure 6. Fault slip distribution of Genaveh earthquake. ZFF are shown too. By extending the causative fault of the earthquake, we reach the ZFF fault line, which indicates that the activity in this seismically thrust active fault at a depth of about 5 km has triggered this earthquake through sedimentary rocks and the existence of alluvial deposits has caused rupture did not reach the surface.

The estimations of the causative fault agree with the previously known local structures, which cut simple sediment folding of Bakhtiari, Lahbari and Aghajari formations (Figure 1) in low folded zone in Dezful Embayment [17,22]. This fault can control the local fault-related folding and the frontal fold growth of large surface anticlines [21].

Despite the highly complex tectonic setting in the Zagros region [38] and the presence of large, active and hidden faults [39] with scattered seismicity [40], which sometimes do not follow the trend of the Zagros folds, we successfully demonstrated that the M_W 5.8 Genaveh mainshock occurred at a shallow dip angle subduction zone, located near the shortening Arabian–Eurasian Plate boundary on the Zagros Foredeep Fault. The used approach can help improve our understanding of the seismic potential of the Zagros region and refine the associated seismic hazards. It does not seem to be distinct from segments of the ZFF that generate steep range front topography elsewhere in the Zagros. According to [22], the deformation had propagated from MFF to Dezful Embayment in the late Miocene and based on our results it still continues.

The orientation of the retrieved fault plane is in good agreement with those published by other international Institutes (Table 1), and is in good agreement with the compressional tectonic regime in the area. The crustal seismicity occurring in the investigated area since 1900 with pure thrust faulting [21,41] is in agreement with our results. Its moment release rate does not greatly exceed those observed either instrumentally or historically and the formers show a seismic behavior similar to the one inferred for this zone [21]. The earthquakes along the ZFF mostly have $\sim 20\text{--}60^\circ$ dipping fault planes that is significantly similar to ours.

The results show that this moderate-size earthquake was located within the sedimentary cover in Zagros with a crustal thickness of ~ 10 km, a basement of ~ 25 km and a Moho depth of ~ 45 km [17,18,42], and does not reach to a Brittle/ Ductile transition zone with predominant dip of $\sim 7^\circ$ [17].

To get more detailed rupture slip distribution, the fault plane is subdivided into subfaults instead of just assuming single fault. As shown in Figure 4, the primary slip mechanism is dip–slip motion concentrated in a single main patch at a depth of 3.5–4.5 km, extending in the strike direction. There is no substantial slip shallower than 2.5 km, which confirms that this earthquake is associated with buried faults.

Even though InSAR is a very powerful instrument, it may not always be appropriate for estimating the effects of low to moderate events, such as earthquakes characterized by magnitudes ranging from 4.5 to <6 . If the signature of the M_W 5.8 mainshock can be attributed to a blind rupture on a pre-existing and known fault, the analysis of the interferograms including the M_W 5.0 aftershock led to no evident conclusion such to attribute the earthquake to known structure. While the extent and amount of signal are

compatible with an M 5.0 event at the expected hypocentral depth, as can be easily verified with a forward model, the deformation patterns cannot be satisfactorily reproduced with the inverse rupture, as expected in this area [1]. It is worth noting that these displacement patterns do not exceed 3 cm and can be significantly altered by the presence of common artifact InSAR sources that would obscure the pure co-seismic offset, or entirely due to surface effects not induced by a shear dislocation.

This earthquake highlights the need for more GPS coverage in this part of Zagros that could help differentiate strain accumulation on a regional low-angle structure and obtain the recurrence time of the main earthquake.

Author Contributions: Conceptualization, Z.G. and N.A.F.; methodology, S.A., Z.G. and N.A.F.; software, Z.G. and N.A.F.; validation, S.A., Z.G., N.A.F. and A.V.; formal analysis, N.A.F. and Z.G.; investigation, Z.G.; resources, N.A.F.; data curation, N.A.F. and Z.G.; writing—original draft preparation, Z.G.; writing—review and editing, Z.G., N.A.F., S.A. and A.V.; visualization, Z.G.; supervision, S.A.; project administration, Z.G.; funding acquisition, N.A.F. All authors have read and agreed to the published version of the manuscript.

Funding: This research received no external funding.

Institutional Review Board Statement: Not applicable.

Informed Consent Statement: Not applicable.

Data Availability Statement: Not applicable.

Acknowledgments: Sentinel data, from the ESA Copernicus Project, were obtained through the Open Access Hub. InSAR processing and data modeling were carried out with SARscape (sarmap, CH).

Conflicts of Interest: The authors declare no conflict of interest.

References

- Berberian, M. Master 'blind' thrust faults hidden under the Zagros folds: Active basement tectonics and surface morphotectonics. *Tectonophysics* **1995**, *241*, 193–224. [CrossRef]
- Agha Nabati, A. *Geology of Iran*; Geological Survey & Mineral Exploration of Iran: Tehran, Iran, 2004.
- IIEES. International Institute of Earthquake and Engineering Seismology. Available online: <http://www.iiees.ac.ir/fa/recentevents> (accessed on 5 May 2021).
- IGUT. Iranian Seismological Center (Institute of Geophysics, University of Tehran). Available online: <http://irsc.ut.ac.ir> (accessed on 5 May 2021).
- Fialko, Y.; Sandwell, D.; Simons, M.; Rosen, P. Three-dimensional deformation caused by the Bam, Iran, earthquake and the origin of shallow slip deficit. *Nature* **2005**, *435*, 295–299. [CrossRef] [PubMed]
- Zebker, H.A.; Rosen, P. On the derivation of coseismic displacement fields using differential radar interferometry: The Landers earthquake. *Int. Geosci. Remote Sens. Symp.* **1994**, *1*, 286–288. [CrossRef]
- Massonnet, D.; Rossi, M.; Carmona, C.; Adragna, F.; Peltzer, G.; Feigl, K.; Rabaute, T. The displacement field of the Landers earthquake mapped by radar interferometry. *Nature* **1993**, *364*, 138–142. [CrossRef]
- Ambraseys, N.N.; Melville, C.P. *A History of Persian Earthquakes*; Cambridge University Press: Cambridge, UK, 1982.
- Hessami, K.; Jamali, F.; Tabasi, H. *Map of Major Active Faults of Iran at 1:2500000*; Seismology Research Center, International Institute of Earthquake Engineering and Seismology (IIEES): Tehran, Iran, 2003.
- Malekzade, Z.; Bellier, O.; Abbassi, M.R.; Shabaniyan, E.; Authemayou, C. The effects of plate margin inhomogeneity on the deformation pattern within west-Central Zagros Fold-and-Thrust Belt. *Tectonophysics* **2016**, *693*, 304–326.
- Eppelbaum, L.V.; Katz, Y.I. A New Regard on the Tectonic Map of the Arabian-African Region Inferred from the Satellite Gravity Analysis. *Acta Geophys.* **2017**, *65*, 607–626. [CrossRef]
- Pollastro, R.M.; Persits, F.M.; Steinshouer, D.W. *Maps Showing Geology, Oil and Gas Fields, and Geologic Provinces of Iran*; U.S. Geological Survey: Reston, VA, USA, 1997. [CrossRef]
- Setudehnia, A.; Perry, J.T. *Genavah 1:100000 Geological Map*; National Iranian Oil Company: Tehran, Iran, 1967.
- Vernant, P.; Nilforoushan, F.; Hatzfeld, D.; Abbassi, M.R.; Vigny, C.; Masson, F.; Nankali, H.; Martinod, J.; Ashtiani, A.; Bayer, R.; et al. Present-day crustal deformation and plate kinematics in the Middle East constrained by GPS measurements in Iran and northern Oman. *Geophys. J. Int.* **2004**, *157*, 381–398. [CrossRef]
- Basilici, M.; Ascione, A.; Megna, A.; Santini, S.; Tavani, S.; Valente, E.; Mazzoli, S. Active deformation and relief evolution in the western Lurestan region of the Zagros mountain belt: New insights from tectonic geomorphology analysis and finite element modeling. *Tectonics* **2020**, *39*, e2020TC006402. [CrossRef]

16. Basilici, M.; Mazzoli, S.; Megna, A.; Santini, S.; Tavani, S. 3-D Geothermal Model of the Lurestan Sector of the Zagros Thrust Belt, Iran. *Energies* **2020**, *13*, 2140. [[CrossRef](#)]
17. Le Garzic, E.; Vergés, J.; Sapin, F.; Saura, E.; Meresse, F.; Ringenbach, J. Evolution of the NW Zagros Fold-and-Thrust Belt in Kurdistan Region of Iraq from balanced and restored crustal-scale sections and forward modeling. *J. Struct. Geol.* **2019**, *124*, 51–69.
18. Pirouz, M.; Avouac, J.-P.; Gualandi, A.; Hassanzadeh, J.; Sternai, P. Flexural bending of the Zagros foreland basin. *Geophys. J. Int.* **2017**, *210*, 1659–1680.
19. Tavani, S.; Parente, M.; Puzone, F.; Corradetti, A.; Gharabeigli, G.; Valinejad, M.; Morsalnejad, D.; Mazzoli, S. The seismogenic fault system of the 2017 Mw 7.3 Iran–Iraq earthquake: Constraints from surface and subsurface data, cross-section balancing, and restoration. *Solid Earth* **2018**, *9*, 821–831. [[CrossRef](#)]
20. Etemad-Saeed, N.; Najafi, M.; Vergés, J. Provenance evolution of Oligocene-Pliocene foreland deposits in the Dezful embayment to constrain Central Zagros exhumation history. *J. Geol. Soc.* **2020**, *177*, 799–817. [[CrossRef](#)]
21. Nissen, E.; Ghods, A.; Karasözen, E.; Elliott, J.R.; Barnhart, W.D.; Bergman, E.A.; Hayes, G.P.; Jamal-Reyhani, M.; Nemati, M.; Tan, F.; et al. The 12 November 2017 Mw 7.3 Ezgeleh-Sarpolzahab (Iran) earthquake and active tectonics of the Lurestan arc. *J. Geophys. Res. Solid Earth* **2019**, *124*, 2124–2152. [[CrossRef](#)]
22. Sun, J.; Sheykh, M.; Windley, B.F.; Talebian, M.; Cao, M.; Ahmadi, N.; Sha, J. Magnetostratigraphic age control of the timing of tectonic deformation and the shifting depositional environments in the Dezful Embayment, Iran. *Tectonics* **2022**, *41*, e2021TC006881. [[CrossRef](#)]
23. Najafi, M.; Vergés, J.; Etemad-Saeed, N.; Karimnejad, H.R. Folding, thrusting and diapirism: Competing mechanisms for shaping the structure of the north Dezful embayment, Zagros, Iran. *Basin Res.* **2018**, *30*, 1200–1229. [[CrossRef](#)]
24. Vergés, J.; Saura, E.; Casciello, E.; Fernández, M.; Villaseñor, A.; Jiménez-Munt, I.; García-Castellanos, D. Crustal-scale cross-sections across the NW Zagros belt: Implications for the Arabian margin reconstruction. *Geol. Mag.* **2011**, *148*, 739–761. [[CrossRef](#)]
25. Sheikholeslami, M.R.; Javadi, H.R.; Sarshar, M.A.; Hoseini, A.A.; Peyma, M.K.; Daneshmand, B.V. *Encyclopedia of Iranian Faults*; Geological Survey and Mineral Exploration of Iran: Tehran, Iran, 2013.
26. Massonnet, D.; Feigl, K.L. Radar interferometry and its application to changes in the earth's surface. *Rev. Geophys.* **1998**, *36*, 441–500. [[CrossRef](#)]
27. Farr, T.G.; Rosen, P.A.; Caro, E.; Crippen, R.; Duren, R.; Hensley, S.; Kobrick, M.; Paller, M.; Rodriguez, E.; Roth, L.; et al. The Shuttle Radar Topography Mission. *Rev. Geophys.* **2007**, *45*, RG2004. [[CrossRef](#)]
28. Goldstein, R.M.; Werner, C.L. Radar interferogram filtering for geophysical applications. *Geophys. Res. Lett.* **1998**, *25*, 4035–4038. [[CrossRef](#)]
29. Costantini, T.M. A novel phase unwrapping method based on network programming. *IEEE Trans. Geosci. Remote Sens.* **1998**, *36*, 813–821. [[CrossRef](#)]
30. Atzori, S.; Hunstad, I.; Chini, M.; Salvi, S.; Tolomei, C.; Bignami, C.; Stramondo, S.; Trasatti, E.; Antonioli, A.; Boschi, E. Finite fault inversion of DInSAR coseismic displacement of the 2009 L'Aquila earthquake (central Italy). *Geophys. Res. Lett.* **2009**, *36*, L15305. [[CrossRef](#)]
31. Okada, Y. Surface deformation due to shear and tensile faults in a half-space. *Bull. Seismol. Soc. Am.* **1985**, *75*, 1135–1154.
32. Williams, C.A.; Wadge, G. The effects of topography on magma chamber deformation models: Application to Mt. Etna and radar interferometry. *Geophys. Res. Lett.* **1998**, *25*, 1549–1552. [[CrossRef](#)]
33. Marquardt, D.W. An Algorithm for Least-Squares Estimation of Nonlinear Parameters. *J. Soc. Ind. Appl. Math.* **1963**, *11*, 431–441. [[CrossRef](#)]
34. Atzori, S.; Manunta, M.; Fornaro, G.; Ganas, A.; Salvi, S. Postseismic displacement of the 1999 Athens earthquake retrieved by the Differential Interferometry by Synthetic Aperture Radar time series. *J. Geophys. Res. Solid Earth* **2008**, *113*, B09309. [[CrossRef](#)]
35. Funning, G.J.; Parsons, B.; Wright, T.; Jackson, J.A.; Fielding, E. Surface displacements and source parameters of the 2003 Bam (Iran) earthquake from Envisat advanced synthetic aperture radar imagery. *J. Geophys. Res. Solid Earth* **2005**, *110*, B09406. [[CrossRef](#)]
36. Wright, T.J.; Lu, Z.; Wicks, C. Source model for the Mw 6.7, 23 October 2002, Nenana Mountain Earthquake (Alaska) from InSAR. *Geophys. Res. Lett.* **2003**, *30*, 18. [[CrossRef](#)]
37. Atzori, S.; Antonioli, A.; Tolomei, C.; De Novellis, V.; De Luca, C.; Monterosso, F. InSAR full-resolution analysis of the 2017–2018 M>6 earthquakes in Mexico. *Remote Sens. Environ.* **2019**, *234*, 111461. [[CrossRef](#)]
38. Alavi, M. Structures of the Zagros fold-thrust belt in Iran. *Am. J. Sci.* **2007**, *307*, 1064–1095. [[CrossRef](#)]
39. Karasözen, E.; Nissen, E.; Bergman, E.A.; Ghods, A. Seismotectonics of the Zagros (Iran) From Orogen-Wide, Calibrated Earthquake Relocations. *J. Geophys. Res. Solid Earth* **2019**, *124*, 9109–9129. [[CrossRef](#)]
40. Madahizadeh, R.; Mostafazadeh, M.; Ansari, A. Long-Term Seismicity Behavior of the Zagros Region in Iran. *Pure Appl. Geophys.* **2016**, *173*, 2637–2652. [[CrossRef](#)]
41. Palano, M.; Imprescia, P.; Agnon, A.; Gresta, S. An improved evaluation of the seismic/geodetic deformation-rate ratio for the Zagros Fold-and-Thrust collisional belt. *Geophys. J. Int.* **2018**, *213*, 194–209. [[CrossRef](#)]
42. Talebian, M.; Jackson, J. A reappraisal of earthquake focal mechanisms and active shortening in the Zagros mountains of Iran. *Geophys. J. Int.* **2004**, *156*, 506–526.